Rock and Soil Mechanics

Volume 44 | Issue 5 Article 5

8-21-2023

Mechanical properties of sand 3D printed rock-like samples based on different post-processing methods

Wei TIAN
School of Civil Engineering, Chang'an University, Xi'an, Shaanxi 710061, China

Xiao-hui WANG
School of Civil Engineering, Chang'an University, Xi'an, Shaanxi 710061, China

Wei YUN
School of Civil Engineering, Chang'an University, Xi'an, Shaanxi 710061, China

Xu CHENG
School of Civil Engineering, Chang'an University, Xi'an, Shaanxi 710061, China

Rock and Soil Mechanics 2023 44(5): 1330−1340 ISSN 1000−7598
https: //doi.org/10.16285/j.rsm.2022.5886 http://rocksoilmech.researchcommons.org/journal

Mechanical properties of sand 3D printed rock-like samples based on different post-processing methods

TIAN Wei, WANG Xiao-hui, YUN Wei, CHENG Xu

School of Civil Engineering, Chang'an University, Xi'an, Shaanxi 710061, China

Abstract: 3D printing, a rapid prototyping technology, has great potential for applications in laboratory rock tests, but the low strength and stiffness of 3D printed samples have been one of the key problems that need to be addressed. In order to find a way to enhance the strength and stiffness of 3D printed rock-like samples, GS19 sand and furan resin were selected as printing materials, and sand 3D printed rock-like samples were used as research objects. Based on this, the samples were post-processed using three different methods: vacuum infiltration, low-temperature treatment, and combination of infiltration and low-temperature. Uniaxial compression tests were carried out on these post-processed sand 3D printed rock-like samples to study their mechanical properties, and the reasons for changes in mechanical properties were analyzed at a microscopic level by scanning electron microscopy. The results indicated that different post-processing methods can change the mechanical properties of the samples, and the combination of infiltration and low temperature can significantly enhance the strength and stiffness of samples, which is related to change in the internal cementation state of samples. The findings of the study can provide new research ideas for future application of 3D printing technology in rock testing.

Keywords: rock mechanics; 3D printing; post-processing method; mechanical properties; microstructure

1 Introduction

Multiple sets of data are required for laboratory tests on rocks to offset experimental errors. However, due to the long-term complex geological and tectonic effects, the internal structure of natural rock cores cannot guarantee a high degree of consistency, thus compromising the accuracy of test data. Additionally, conducting research on prefabricated flaws requires cutting them in natural rocks. Traditional cutting methods (such as carving machines and water jet cutting) are not only difficult to cut out the complex prefabricated flaws, the microcracks generated during the cutting process will affect the reliability of the test results.

To avoid difficulties in obtaining natural rocks and prepare prefabricated flaws, rock-like materials have become one of the main models for rock laboratory tests. However, traditional methods have limitations in making rock-like models; for example, manually mixed materials may be inhomogeneous, complex flaws are difficult to create, and manual operations cannot guarantee the precision of flaws. Therefore, how to obtain a large number of highly rock samples with consistent complex structural has always been one of the key issues that need to be addressed in rock laboratory tests.

3D printing technology can effectively prepare complex structural samples with high precision, short production cycles and customization. This technology has attracted widespread attention and has been applied to the field of rock mechanics by many scholars[1–5]. Currently, liquid photosensitive resin materials and powder materials such as gypsum and sand are mainly used for producing rock-like samples using 3D printing technology. Liquid photosensitive resin materials use stereolithography technology to rapidly solidify by irradiating with ultraviolet laser beams. The printed sample has a high degree of transparency which helps visualize internal stress evolution and crack propagation in rocks [6–8]. Powder materials are bonded by binders. Sand 3D printing material is close to the mineral particles inside natural rocks and bonding components. This printing method mainly produces samples by using furan resin and sand powder in a certain proportion, and the obtained samples are similar in structure to natural rocks, where the particles are connected into a whole by bonding material. This method of forming a three-dimensional solid by bonding resin and sand powder layer by layer is regarded to be a reasonable method for making rock-like samples. Kong et al. [9] employed back-scattered scanning electron microscopy (BS-SEM) and energy dispersive spectroscopy (EDS) to identify the particles, filling forms, and bonding materials of sand 3D printed rock-like samples so as to determine its microstructure. They pointed out that in terms of pore structures, using sand 3D printed rock-like samples to replace natural rocks for physical tests is feasible but still needs to improve the similarity of pore structures and mechanical properties. Gomez et al. [10] studied the mechanical behavior and permeability evolution of sand 3D printed rock-like samples under different confining pressures through triaxial unconsolidated-

Received: 13 June 2022 Accepted: 15 July 2022
This work was supported by The Youth Innovation Team of Shaanxi Universities (Disaster Mechanism and Safety Control of Underground Engineering in Complex Geotechnical Environment).
First author: TIAN Wei, male, born in 1981, PhD, Professor, PhD supervisor, research interests: numerical simulation of geotechnical engineering and micromechanical analysis of geotechnical materials. E-mail: tianwei@chd.edu.cn
Corresponding author: WANG Xiao-hui, male, born in 1998, Master, focusing on application of 3D printing technology in geotechnical engineering. E-mail:1278876874@qq.com

drained tests. The test results indicated that sand 3D printing technology can produce rock-like samples with mechanical behavior similar to natural reservoir rocks but there are still differences. Qi et al. [11] used digital image correlation (DIC) method to perform non-contact deformation measurement on sand 3D printed rock-like samples with different joint densities for studying the evolution law of strain field and strain localizations as well as the growth of new cracks during loading.

Our research team has conducted extensive studies using combined CT scanning and 3D printing technology to produce sand 3D printed specimens with internal structures similar to natural rocks. In order to apply 3D printing technology to the field of rock mechanics, our team has investigated the mechanical properties and crack propagation of sand 3D printed specimens under high temperature conditions, as well as the dynamic mechanical properties and energy dissipation laws under impact loads that are commonly encountered in practical engineering[12–14].

However, all of these studies face a common problem: the low strength and stiffness of the sand 3D printed material limit its ability to replicate natural rocks. Currently, sand 3D printed specimens are suitable for simulating weak rocks with low compaction degree, poor particle bonding, and low structural strength, but cannot be used for larger-scale research [4,15]. Therefore, in order to meet the demand for replicating natural rocks, it is necessary to significantly improve the strength and stiffness of the sand 3D printing material.

Since the microstructure characteristics of rock materials govern their macroscopic physical and mechanical properties, pore structures and cementitious materials have an important influence on their mechanical properties [16–19]. Based on this, furan resin and sand powder materials were employed to create sand 3D printed specimens. Then these specimens were post-processed through three methods: vacuum infiltration, low-temperature treatment, and combined infiltration at low temperature. Mechanical tests on standard specimens before and after treatment were conducted, and their microstructural changes were analyzed using scanning electron microscopy. This study provides solutions and ideas for addressing the low strength and stiffness of sand 3D printed specimens.

2 Specimen preparation

2.1 Sand 3D printed rock-like samples

The experiment utilized the 3DP technology to print the initial samples using a VX1000 3D printer with a minimum printing thickness of 0.20–0.30 mm. The printer powder and binder used were GS19 sand and furan resin, respectively, which are compatible with the printer. The main mineral component of GS19 sand is quartz, with a uniform particle size distribution between 0.20–0.35 mm. Furan resin is a commonly used thermosetting adhesive that exhibits good compatibility compared with other resins and is often used in casting processes. The printer and materials are shown in Fig.1.

The dimensions of the 3D printed rock-like samples accorded with the recommendations of the International Society of Rock Mechanics (ISRM). A cylindrical model measuring ϕ50 mm×100 mm was created using computer-aided design software Rhino. The model was exported in stereo lithography (STL) format, which contains geometric information about the sample that can be recognized by the 3D printer. After recognizing the three-dimensional structure digital model, sand powder was sequentially laid out according to the design layer thickness (0.4 mm), and then solid printing was implemented layer by layer in a powder-binder-powder-binder form. Since printing direction affects mechanical properties of samples, *Z*-direction was defined as positive direction for printing in this study. After forming, residual powder on the surface of samples was cleaned up. The sample preparation method is consistent with that used by our research team previously and will not be further elaborated here; and specific printing procedures are presented in Fig. 2.

(a) VX1000 3D printer

(b) GS19sand

(c) Furan resin

Fig. 1 Machine and material of sand 3D printed specimens

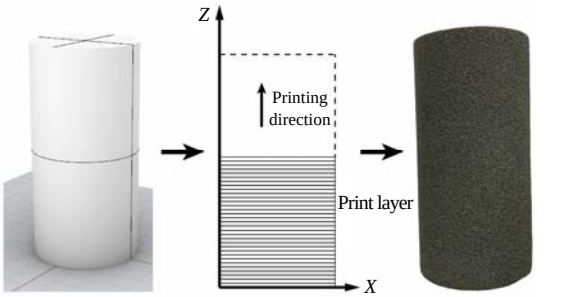

(a) Digital model (b) Print process (c) Physical specimens

Fig. 2 Printing process

2.2 Post-processing methods

Following the post-treatment methods proposed by Wu et al.[20] and Mostafaei et al.[21], the polyether

amine epoxy resin adhesive (epoxy adhesive in following paragraphs) was selected as an infiltrant to treat the specimens using vacuum infiltration in this study, based on a comprehensive comparison of its flowability, initial curing time, and storage time. The epoxy adhesive consists of two components, A and B. Component A is the epoxy resin matrix, which is white and viscous, while component B is a polyether amine curing agent that is light yellow and has good fluidity. Components A and B are uniformly mixed in a 2:1 ratio provided by the supplier before curing begins. The curing time is affected by temperature, with an initial curing time of 2 h at room temperature (25℃). Additionally, since organic resins are temperature-dependent materials, their mechanical properties are affected by temperature [22]. To enhance the brittleness of 3D printed rock-like samples, carbon ice was used for low-temperature treatment based on the method of Zhou et al [23].

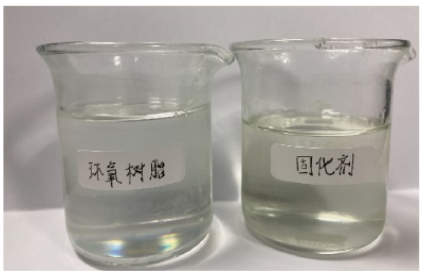

Fig. 3 Polyether amine epoxy resin adhesive

To investigate the effects of different post-processing methods on the mechanical properties of sand 3D printed rock-like samples, the printed samples by different post-processing methods were divided into four experimental groups: BC group, PI group, PT group, and PIT group, with five samples in each group. BC represents the blank control group, P represents post-processing, I represents vacuum infiltration, and T represents low-temperature treatment. The detailed processing methods for each group are as follows:

(1) BC Group: After printing, the samples were dried in a constant-temperature drying oven and stored at room temperature without further treatment.

(2) PI Group: This group was used to study the effect of infiltration treatment at room temperature on the mechanical properties of the samples. Due to the viscosity and limited curing time of epoxy resin adhesive, directly draining through a connecting pipe will lead to blockage of the pipe. The method shown in Fig. 4 was used to uniformly infiltrate the epoxy resin adhesive into the sample. ①Place the inner container containing 3D printed rock-like samples and prepared epoxy resin adhesive in a sealed bucket connected to a vacuum pump and immerse the sample with epoxy resin adhesive (Fig. 4(a)). ② Close other valves, turn on the vacuum pump and corresponding connection valve for 10 minutes to extract air from the bucket. After the pressure gauge stabilizing, maintain a vacuum environment inside the bucket for 10 minutes. Then, initiate the preliminary infiltration process by utilizing the pressure differential between the interior and exterior of the specimen, as well as capillary action. ③ Close valves and vacuum pump, open the valve connected to atmosphere, thus atmospheric pressure can drive epoxy resin adhesive into deep pores of samples (Fig. 4(c)). ④ Take out inner container, add epoxy resin adhesive again until the sample is submerged, and then put the inner container back into the bucket (Fig. 4(d)). Repeat steps ②–④ until there is no significant change in sample mass. Finally, wipe off excess epoxy resin adhesive on the surface of the sample and place it in a constant-temperature drying oven until it is completely cured.

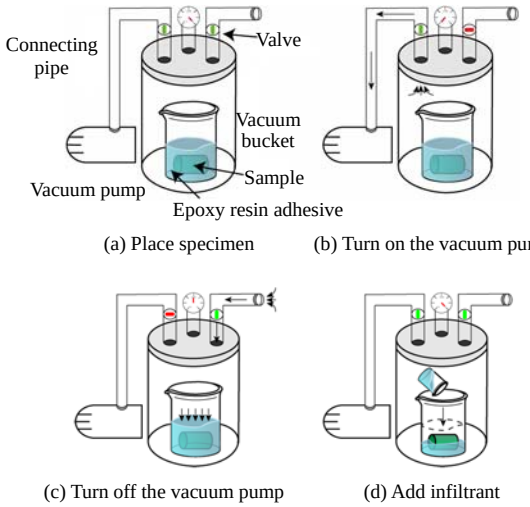

Fig. 4 Vacuum infiltration process

(3) PT group: Prior to conducting the uniaxial compression test, the untreated specimens were buried in an insulated box filled with carbon ice, as shown in Fig. 5. Temperature measurements were taken every 2 h during the freezing period to maintain a constant environment temperature of –70 ℃ for the specimen. The specimen was dislodged from the low-temperature environment after a minimum freezing time of 24 h for conducting the uniaxial compression test.

Fig. 5 Low-temperature treatment

(4) PIT group: To compare the effect of temperature on epoxy resin adhesive, a combined infiltration and low-temperature treatment method was used for specimen treatment. The combined infiltration and low-temperature methods were the same as those used in PI and PT groups. The specimen was first subjected to infiltration and then buried in an insulated

box filled with carbon ice for low-temperature treatment after solidification.

Figure 6 depicts 3D printed rock-like samples from various experimental groups.

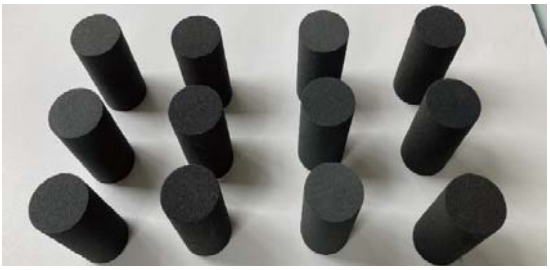

BC group PI group PT group PIT group

Fig. 6 3D printed rock-like samples

2.3 Experimental program

Uniaxial compression tests and scanning electron microscopy tests were conducted on samples from different experimental groups. The effects of different post-processing methods on the mechanical properties of sand 3D printed rock-like samples were evaluated through mechanical tests, and microscopic structure studies was carried out to analyze the mechanism underlying the variations in mechanical properties.

The WAW31000 microcomputer servo universal testing machine was used for the uniaxial compression test with a loading rate of 0.05 mm/s. Axial deformation was recorded by the built-in sensors of the testing machine. Prior to loading, polytetrafluoroethylene sheets were placed between both ends of the sample and the pressure plate of the apparatus to reduce friction, and a baffle was used during testing for protection.

The Zeiss Merlin Compact electron microscope scanner was employed to scanning microscopic structure with magnification between 50–1000 and scanning voltage between 1.0–2.0 kV. The experimental equipment is depicted in Fig. 7.

(a) WAW31000 microcomputer servo universal testing machine

(b)Zeiss Merlin Compact electron microscope scanner

Fig. 7 Experimental equipment

3 Results and analysis

3.1 Variations in appearance and mass

After different post-treatments, the appearance of sand 3D printed rock-like samples underwent various changes, as shown in Fig. 8. It can be observed that the apparent color of the samples in BC group is dark brown, with slight sand particle peeling phenomenon on the surface. After infiltration treatment, the apparent color of PI specimens changed to gray-black, and the peeling phenomenon disappeared. The samples subjected to low-temperature treatment had a white frost layer attached to their outer layer, and the peeling phenomenon was reduced to some extent.

(a) BC group (b) PI group (c) PT group

Fig. 8 Appearance contrast

The mass variations of sand 3D-printed rock-like samples in each group are listed in Table 1. The treated specimens exhibit a significant increase in mass and density, with the incremental mass originating from the epoxy resin infiltrated into the specimen. The mass of the specimens subjected to low-temperature treatment has slightly increased due to the adhesion of moisture from the air onto the specimen surface. Additionally, Table 1 reveals that the mass of untreated sand printed rock-like samples is very similar, and that the changes in mass by post-processing are also essentially identical. This indicates that not only do rock-like samples prepared through 3D printing technology show a similar appearance, but also that sand printed rock-like samples using identical digital models exhibit a high degree of internal consistency.

Table 1 Mass changes of 3D printed rock-like samples by different post-processing

Post-processing methods	Average mass before processing /g	Average mass after processing /g	Mass variations /g	Average density /(g·cm^{-3})
BC Group	281.632	281.632	—	1.434
P I Group	281.156	373.057	91.901	1.900
PT Group	281.375	283.796	2.421	1.445
PIT Group	281.782	375.297	93.515	1.911

3.2 Effects of post-processing methods on mechanical properties and failure modes

3.2.1 Stress–strain relationships

Uniaxial compression tests were conducted on cylindrical samples for each group, and the strength

and elastic modulus variations were thus obtained. Table 2 lists the uniaxial compression test results for each group of samples and corresponding mean values.

Table 2 Results of uniaxial compression tests

Specimen type	No.	Yield strain /10^{-3}	Peak strain /10^{-3}	Yield strength /MPa	Peak strength /MPa	Elastic modulus /GPa
BC Group	BC-1	6.74	7.55	5.41	5.80	0.96
	BC-2	4.81	8.00	4.66	6.67	1.30
	BC-3	5.07	7.58	4.74	6.04	0.98
	BC-4	6.03	8.12	5.52	6.58	0.82
	BC-5	4.10	7.30	4.52	5.76	0.89
	Mean	5.35	7.71	4.97	6.17	0.99
PI Group	PI-1	11.73	20.77	9.38	11.05	0.88
	PI-2	13.78	23.02	9.80	12.57	0.95
	PI-3	12.30	21.62	9.44	12.00	0.94
	PI-4	12.11	21.14	9.57	11.88	0.90
	PI-5	12.63	22.20	9.69	12.45	0.93
	Mean	12.51	21.75	9.58	11.99	0.92
PT Group	PT-1	6.41	6.56	13.59	13.92	3.70
	PT-2	6.11	6.55	11.90	13.54	4.88
	PT-3	6.33	6.81	11.92	13.60	4.39
	PT-4	6.90	7.41	12.11	14.19	4.56
	PT-5	5.85	6.52	10.53	13.00	4.12
	Mean	6.32	6.77	12.01	13.65	4.33
PIT Group	PIT-1	12.39	12.94	185.37	195.43	30.78
	PIT-2	12.24	13.11	180.29	190.51	25.77
	PIT-3	11.84	13.02	180.11	192.95	25.51
	PIT-4	11.95	13.25	188.06	196.15	25.33
	PIT-5	11.58	12.88	185.47	194.16	23.16
	Mean	12.00	13.04	183.86	193.84	26.11

Table 2 reveals significant changes in the mechanical properties of the processed samples compared to the control group. Specifically, the average strength of the PI group reached 11.99 MPa, which is 94.3% higher than that of the control group. The average elastic modulus slightly decreased from 0.99 GPa to 0.92 GPa, indicating that infiltration treatment can improve the strength of 3D printed rock-like samples to some extent, but also lead to a slight decrease in stiffness due to the toughness exhibited by the infiltrant fluid, making samples more prone to deformation. Meanwhile, the PT group showed a remarkable increase in both average strength and average elastic modulus, reaching 13.65 MPa and 4.33 GPa, respectively, with an increment by 121.2% and 337.4%. This suggested that low-temperature treatment remarkably enhances the brittleness of samples. The most significant changes were observed in PIT group, with an increase in average strength and average elastic modulus up to 193.84 MPa and 26.11 GPa by 3041.7% and 2537.4%, respectively. This indicates that combined infiltration and low-temperature treatment have a prominent effect on the strength and stiffness of samples.

Figure 9 displays typical stress–strain curves of different post-processed samples under uniaxial compression, where distinct differences can be observed in their mechanical properties after various treatments are applied. The stress–strain curves for BC group, PT group and PIT group showed consistent behavior during the pre-peak stage. At the initial loading stage, all curves exhibited an upward concave compaction segment (corresponding to OA_1, OA_3 and OA_4 segments respectively), as microcracks inside specimens were closed. OA_1 segment was shorter than other two segments, indicating that low-temperature treatment increased the number of microcracks inside samples. After the concave segment, stress–strain curves entered a linearly elastic stage (A_1B_1, A_3B_3 and A_4B_4 segments) until reaching the yield point. Post-yield curves showed a downward convex plastic stage (B_1C_1, B_3C_3 and B_4C_4 segments), with B_3C_3 segment exhibiting a greater increase in stress but smaller increase in strain than B_1C_1 segment, indicating again that low-temperature treatment enhances the brittleness of samples. All three groups exhibited brittle failure. However, their post-peak behaviors differed: PT group and PIT group show a sharp drop after peak stress, leading to an immediate loss of load-bearing capacity; whereas the post-peak curves of group BC exhibits a piecewise linear pattern, indicating that the sample still possesses a certain level of load-bearing capacity after the peak strength.

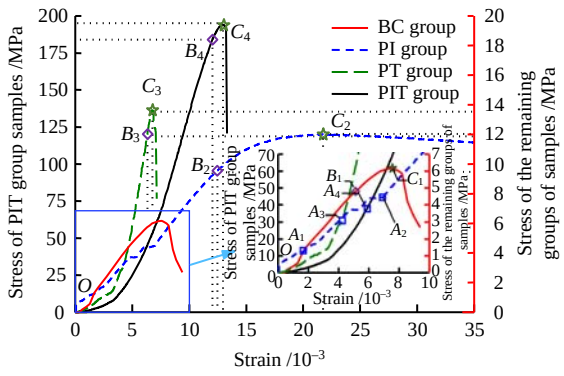

Fig. 9 Stress-strain curves of 3D printed rock-like samples after different post-processing methods

The stress–strain curve of the PI group sample treated with infiltration was distinctly different from the other three groups. At the OA_2 stage, the PI group curve consisted of multiple segments of broken lines without an obvious upper concave section, indicating that the internal pores of the sample were filled with epoxy resin adhesive. After the OA_2 stage, the curve entered a linear elastic stage (A_2B_2 segment), which was characterized by a straight line. Subsequently, the curve entered a plastic section (B_2C_2 segment) with a downward concave shape, and this stage had a significantly larger strain range than that of the plastic section of other three groups. There was no prominent drop in the curve after reaching its peak point, and the sample exhibits plastic failure, which is different from brittle failure of natural rocks. The reason for this phenomenon is that epoxy resin infiltration can change the mechanical properties of samples from brittle to plastic.

3.2.2 Failure pattern

The failure patterns of 3D printed rock-like samples using various post-processing methods are shown in Fig. 10. It can be observed that the failure modes of

the samples can be divided into tensile and shear types. Under uniaxial compression, small cracks parallel to the loading direction were first generated at the ends of samples in the BC group, which gradually extended to form axial splitting failure accompanied by powder falling off. The PI samples treated with infiltration exhibited obvious lateral expansion deformation during uniaxial compression, with inclined shear cracks appearing on the surface. Meanwhile, their color gradually changed to brown and the end surfaces turned white due to the extrusion of epoxy resin adhesive under compression. The failure mode of the PT samples treated at low temperature was also axial splitting failure, with more obvious tensile cracks compared to the BC group. The PIT samples treated with both infiltration and low-temperature exhibited mainly axial splitting failure and partial shear failure as a secondary mode. During failure, there was a loud noise and the sample broke into pieces, showing similar changes on their surfaces as those in PI samples, with some fracture surfaces appearing white.

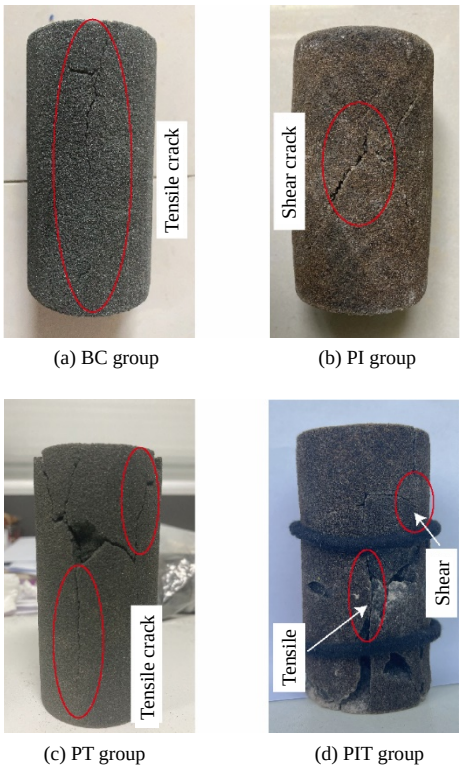

(a) BC group (b) PI group

(c) PT group (d) PIT group

Fig. 10 Failure modes of 3D printed rock-like samples by different post-processing methods

3.2.3 Post-processing effects

Different post-processing methods have significantly altered the mechanical and deformation properties of 3D printed rock-like samples. The main reasons for this are the bonding mechanisms between particles, the composition of bonding materials, and temperature. The samples of BC group were printed using a method commonly adopted in sand casting molds, where the amount of furan resin used was limited to reduce gas generation and ensure the quality of castings. This factor led to weak interparticle bonding in conventional samples, resulting in low macroscopic strength. By infiltrating with epoxy resin, the pores in the sample were filled, and the bonding material between particles was dominated by epoxy resin, leading to increased strength in sand 3D printed rock-like samples. However, using polyether amine as a curing agent for epoxy resin enhances toughness after curing, resulting in obvious plastic features after compression. After low-temperature treatment, the mobility of bonding material decreased, and relative particle displacement was restricted, requiring more external force to cause damage. Therefore, the samples of PT group and PIT group exhibited increased strength and obvious brittle features.

3.2.4 Comparison of mechanical properties and failure modes

Based on experimental results from Refs. [24–28], stress–strain curves and failure modes between low-temperature treated samples and weakly bonded coarse-grained sandstone as well as between samples treated by combination of infiltration and low temperature and granite in uniaxial compression tests were compared.

3.2.4.1 Comparison of mechanical properties

From Fig. 11(a), it can be observed that the stress–strain curve of the PT samples treated at low temperature is similar to that of the weakly cemented coarse-grained sandstone under uniaxial compression conditions. The peak stress, peak strain, and elastic modulus are relatively close, indicating a high similarity between the low-temperature treated samples and weakly cemented coarse-grained sandstone. By comparing the mechanical properties in Table 3, it can be seen that the uniaxial compressive strength and elastic modulus of the PIT samples treated by combination of infiltration and low-temperature are smaller than that of granite. Furthermore, comparing the stress–strain curves of the PIT specimens in Fig. 11(b) with those of granite in Refs. [26–28], it can be found that their overall trend and stages are similar, and their peak strains are also at a similar level with that of natural granite. Therefore, it can be concluded that these post-treated specimens have certain similarities with granite in terms of mechanical properties.

3.2.4.2 Comparison of failure modes

Figure 12 compares the failure modes of the post-processed specimens and natural rocks under uniaxial compression conditions. By comparisons in Fig. 12(a) and Fig. 12(b), it can be seen that the failure mode of the PT samples treated at low temperature is similar to that of weakly cemented coarse-grained sandstone, where macroscopic main cracks in both samples are tensile cracks, with secondary cracks generated during loading. Figs. 12(c) and 12(d) show the failure modes of the PIT samples processed by combined infiltration and low-temperature and granite samples, respectively. They both exhibit combined tensile-shear failure,

presenting as blocky after failure.

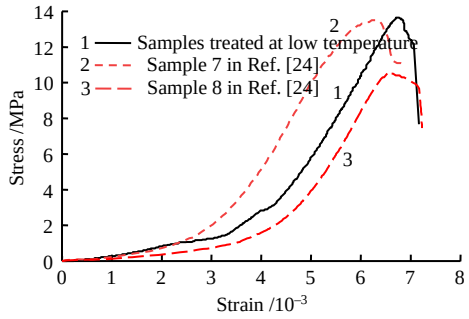

(a) Comparison of stress–strain curves between PT samples and weakly cemented coarse-grained sandstone [24].

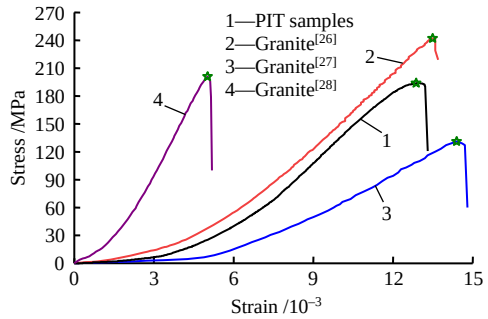

(b) Comparison of stress–strain curves between PIT samples and granite

Fig. 11 Comparison of stress–strain curves between 3D printed rock-like samples by different post-processing and natural rocks

Table 3 Comparison of mechanical properties between samples processed by combined infiltration and low-temperature and granite

ample type	Uniaxial compressive strength /MPa	Elastic modulus /GPa
PIT samples treated by combined infiltration and low-temperature	193.84	26.11
Granite[26]	242.81	20.20
Granite[27]	132.15	14.79
Granite[28]	206.58	53.28

By comparing the stress–strain curves and failure modes, it can be found that the mechanical properties and failure modes of post-processed sand 3D printed rock-like samples are similar to those of natural rocks. However, it should be noted that 3D printed rock-like samples typically possess a layered structure along the printing direction due to the printing process, which is currently the main structural difference between 3D printed samples and natural rocks. In this study, a single printing direction was set. When the loading direction is parallel to this printing direction, the mechanical characteristics of unprocessed samples are closer to those of natural rocks. Additionally, it is found that combined infiltration and low-temperature method can improve sample density and make mechanical properties similar to those of granite. However, since only one printing direction was set in this experiment, further research needed to determine whether the mechanical properties and failure modes of post-processed samples are still affected by the layered structure caused by the printing direction. Our research team will continue to explore the feasibility of using post-processing methods to eliminate the effect of layered structures on the mechanical properties of printed samples.

(a) Failure mode of PT samples (b) Failure mode of weakly cemented coarse-grained sandstone[25]

(c) Failure mode of PIT samples (d) Failure mode of granite[26]

Fig. 12 Comparison of failure modes between 3D printed rock-like samples by different post-processing and natural rocks

3.3 Microscopic mechanism analysis

Scanning electron microscopy experiments were conducted on 3D-printed rock-like samples treated with different post-processing methods. The magnification was set between 50 and 500 times to observe the overall morphology of the fracture surface, as well as the particle shapes, cementitious morphology, and inter-particle cementation within the fracture surface, as shown in Fig. 13.

The SEM images of the BC samples at different magnifications are shown in Figs. 13(a) and 13(b). The overall morphology of the sample fracture surface shows that particles are clearly visible with obvious inter-particle pores. Figure 13(b) reveals that the untreated BC samples have a layer of furan resin film attached to the surface of sand particles. The particles are interlocked with each other. At the protruding parts of interlocking, there is furan resin bonding, which belongs to a "point-to-point" contact mode. This is consistent with the analysis of low strength at the macro level.

The SEM images of PI samples are shown in Figs. 13(c) and 13(d). It can be observed from Fig. 13(c) that particles are not easily distinguishable, and epoxy resin fractures and separates from sand particles to form voids inside the material. At a high magnification

in Fig. 13(d), some branches of epoxy resin extending outward from particle connections and partially uncoated particles can be observed, indicating that PI samples treated by vacuum infiltration no longer have furan resin cementation between particles but instead have overall filling of epoxy resin into inter-particle pores.

The SEM images of the PT samples after low-temperature treatment are presented in Figs. 13(e) and 13(f). At a low magnification in Fig.13(e), the overall morphology of the PT sample particles is similar to that of the BC group, and particles and pores can be clearly observed. At a higher magnification, however, the furan resin on the surface of the particles exhibits more wrinkles and becomes rough. Moreover, cracks are generated in local areas on the surface of particles.

The SEM images of the PIT samples after infiltration and low-temperature treatment are shown in Figs. 13(g) and 13(h). The microstructure is significantly different from those of other groups. In Fig. 13(g), compared with PI samples treated by infiltration at room temperature, the particles are more tightly packed together, making them difficult to be distinguished from each other under epoxy resin encapsulation. The pores formed by detachment between resin and particles are significantly reduced. In Fig.13(h), sand particles are completely encapsulated by epoxy resin. Different from that at room temperature, the fracture surfaces at particle connections are flat and shear failure occurs.

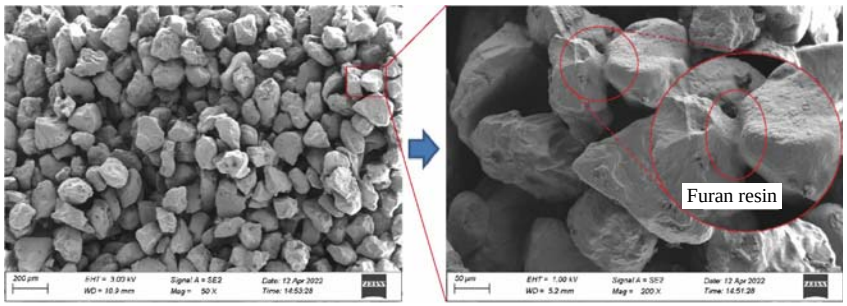

(a) Microscopic morphology of the fracture surface of BC samples (b) Morphology of particles in BC samples

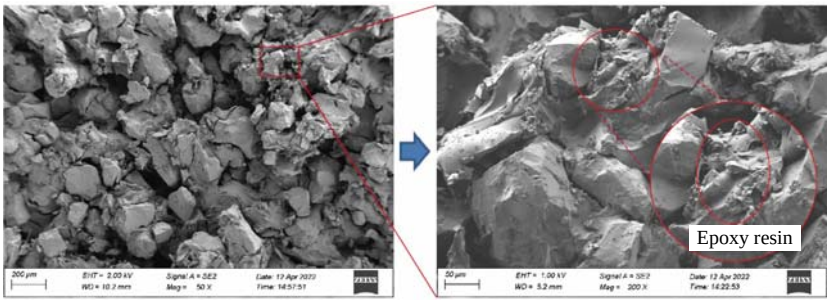

(c) Microscopic morphology of the fracture surface of PI samples (d) Morphology of particles in PI samples

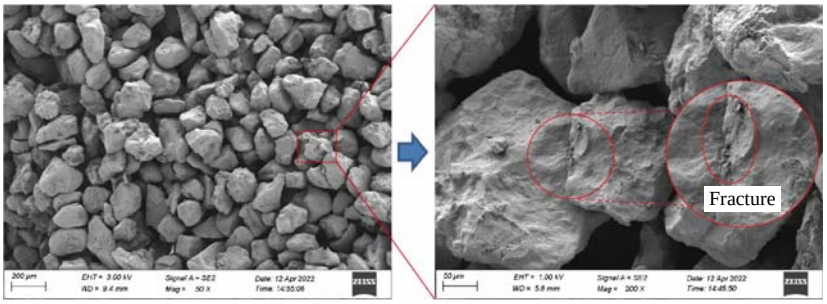

(e) Microscopic morphology of the fracture surface of PT samples (f) Morphology of particles in PT samples

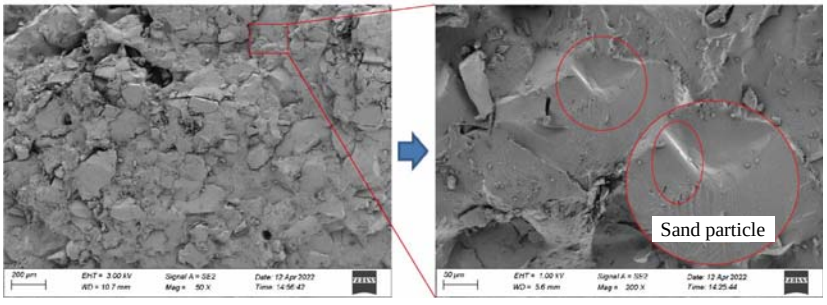

(g) Microscopic morphology of the fracture surface of PIT samples (h) Morphology of particles in PIT samples

Fig. 13 Electron microscopic scanning images of 3D printed rock-like samples by different post-processing

Figure 14 illustrates schematic diagrams of particle connections and failure patterns for different samples based on SEM results. As shown in Fig. 14(a), furan resin of samples in the BC group first bears external loads before failure. Then relative displacement occurs between particles, and external forces gradually shift to mechanical interlocking forces and frictional forces between particles. With further increase in external force, microcracks emerge inside samples and continue to expand to result in final failure. The content of bonding material between particles has an important effect on the mechanical properties of samples during compression. Weak "point-to-point" contacts lead to a lower strength for sand 3D printed rock-like samples than for samples of other groups.

Figure 14(b) presents the particle connections and failures of PI samples. External forces are borne by epoxy resin between particles, while the epoxy resin is deformed when relative displacement occurs between particles, and finally, the resin breaks under tension. Some fractures occur at the weak bonding on the particle surface, causing detachment between epoxy resin and sand particles, which results in holes. Epoxy resin has higher tensile strength than furan resin and has certain toughness under the action of polyether amine. Even if there is a large change in position between particles, their connection is difficult to break, so the uniaxial compression strength of samples is improved, and obvious plasticity is observed as indicated by the stress–strain curve in Fig. 9.

The mechanical property variations of PT samples after low-temperature treatment are caused by the increased strength of furan resin and uneven shrinkage of furan resin on the surface of particles. As shown in Fig. 14(c), low-temperature treatment causes internal shrinkage and stress in furan resin. Once internal stress exceeds the strength of furan resin, it will result in resin failure and the appearance of cracks. However, the strength of resin materials increases as the temperature decreases. At low temperatures, the mobility of polymer chains within the furan resin is reduced, requiring more external energy to rupture the furan resin. Additionally, when the furan resin is broken, the rough surface of the particles increases friction between them, further enhancing the strength of the sample.

The particle morphology and failure of PIT samples after combined infiltration and low-temperature treatment are shown in Fig.14(d). From a micro perspective, low temperature mainly enhances the overall integrity of sand particle–epoxy resin composite system. Low temperature causes shrinkage in epoxy resins which strengthens bonding between particles and resins. Polymer chains are restricted from movement at low temperatures, resulting in shorter distances between molecules and increased intermolecular forces. Hence, more energy is required to break the resin, particles and bonding interface between resin and particles. The failure of PIT samples is mainly due to detachment between resin and particles, shear damage to resin between particles, and fracture of particles themselves.

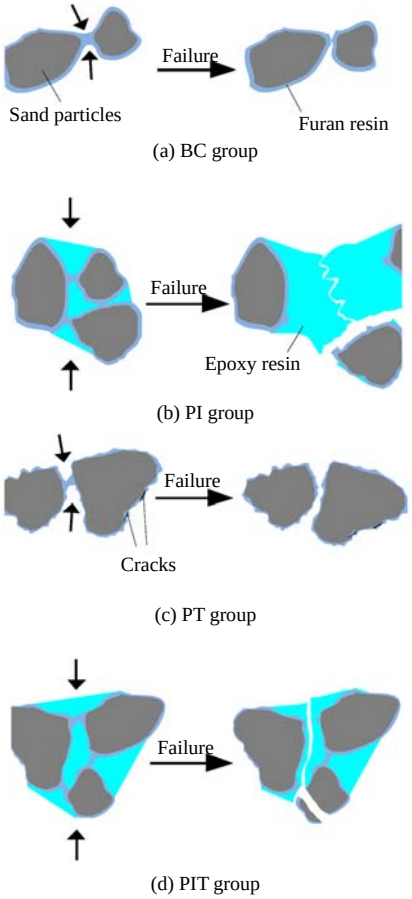

Fig. 14 Diagrams of particle connection and failure of 3D printed rock sample by different post-processing

4 Conclusions

The sand 3D printed rock-like samples were post-processed using vacuum infiltration, low-temperature treatment, and combination of infiltration and low-temperature. Subsequently, uniaxial compression tests and scanning electron microscopy experiments were conducted on these samples. The results indicate that:

(1) Various post-processing methods can enhance the strength of sand 3D printed rock-like samples, with the combined low-temperature and infiltration method showing the most significant improvement.

(2) Post-processing can alter the stress–strain relationship and failure mode of 3D printed rock-like samples. The vacuum-infiltrated samples exhibits significant plastic deformation during compression due to the inherent deformation properties of epoxy resin. The mechanical properties of low-temperature treated samples are similar to those of weakly cemented coarse-grained sandstone, while those treated with combined infiltration and low-temperature shows mechanical properties similar to granite.

(3) Prominent changes in microtopography of samples are observed before and after processing. Untreated samples has visible particles with numerous pores between them. After infiltration, the inter-particle pores are filled with epoxy resin, resulting in the

increase in the bonding area between particles. After low-temperature treatment, the mobility of resin is reduced, friction between uninfiltrated particles is increased, and integrality of infiltrated particles and resin is enhanced, resulting in increased strength.

5 Outlook

Through various post-processing methods, it is possible to overcome the limitations of low strength and stiffness in sand 3D printed rock-like samples to a certain extent, achieving a larger range of natural rock replication, which is conducive to the application of 3D printing technology in rock laboratory testing. However, current research still has some limitations:

(1) 3D printed rock-like samples typically exhibit a layered structure along the printing direction, which greatly affects their mechanical properties and failure modes. Our research team will investigate whether post-processed samples are still affected by the layered structure by preparing post-processed samples with different printing directions.

(2) Low-temperature treatment can improve the brittleness of sand 3D printed rock-like samples, but natural rocks usually cannot adapt to extremely low ambient temperatures. The next step in research is to develop new infiltrants that can enhance strength and stiffness at room temperature for samples treated by vacuum infiltration.

(3) Defects such as joints and fissures in natural rocks, which are formed by geological processes, increase the complexity of deformation and stress distribution under complex stress conditions. With the advantages of highly accurate reproduction and rapid replication of complex structures offered by 3D printing technology, the focus of our research team will be on studying crack propagation and damage evolution in flawed samples after post-processing.

References

[1] LIU Quan-sheng, HE Fan, DENG Peng-hai, et al. Application of 3D printing technology in physical modelling in rock mechanics[J]. Rock and Soil Mechanics, 2019, 40(9): 3397–3404.

[2] TIAN Wei, YU Chen, ZHANG Li. Application of 3D printing technology in rock mechanics[J]. Mechanics in Engineering, 2021, 43(2): 181–189.

[3] WANG Chong-lang, QI Sheng-wen. Application and prospect of 3D printing for rock mechanics[J]. Progress in Geophysics, 2018, 33(2): 842–849.

[4] GAO Y T, WU T H, ZHOU Y. Application and prospective of 3D printing in rock mechanics: a review[J]. International Journal of Minerals, Metallurgy and Materials, 2020, 28(1): 1–17.

[5] HUANG Na, JIANG Yu-jing, CHENG Yuan-fang, et al. Experimental and numerical study of hydraulic properties of three-dimensional rough fracture networks based on 3D printing technology[J]. Rock and Soil Mechanics, 2021, 42(6): 1659–1668, 1680.

[6] XIE He-ping, GAO Feng, JU Yang. Research and development of rock mechanics in deep ground engineering[J]. Chinese Journal of Rock Mechanics and Engineering, 2015, 34(11): 2161–2178.

[7] JU Y, REN Z Y, ZHENG J T, et al. Quantitative visualization methods for continuous evolution of three-dimensional discontinuous structures and stress field in subsurface rock mass induced by excavation and construction—an overview[J]. Engineering Geology, 2020, 265: 105443.

[8] ZHOU T, ZHU J B, XIE H P. Mechanical and volumetric fracturing behaviour of three-dimensional printing rock-like samples under dynamic loading[J]. Rock Mechanics and Rock Engineering, 2020, 53(6): 2855–2864.

[9] KONG L Y, OSTADHASSAN M, HOU X D, et al. Microstructure characteristics and fractal analysis of 3D printed sandstone using micro-CT and SEM- EDS[J]. Journal of Petroleum Science and Engineering, 2019, 175: 1039–1048.

[10] GOMEZ J S, CHALATURNYK R J, ZAMBRANO-NARVAEZ G. Experimental investigation of the mechanical behavior and permeability of 3D printed sandstone analogues under triaxial conditions[J]. Transport in Porous Media, 2019, 129(2): 541–557.

[11] QI Fei-fei, ZHANG Ke, XIE Jian-bin. Fracturing mechanism of rock-like specimens with different joint densities based on DIC technology[J]. Rock and Soil Mechanics, 2021, 42(6): 1669–1680.

[12] TIAN Wei, YU Chen, WANG Xiao-hui, et al. A preliminary research on dynamic mechanical properties and energy dissipation rule of 3D printed fractured rock[J]. Chinese Journal of Rock Mechanics and Engineering, 2022, 41(3):446–456.

[13] TIAN Wei, WANG Zhen, ZHANG Li, et al. Mechanical properties of 3D printed rock samples subjected to high temperature treatment[J]. Rock and Soil Mechanics, 2021, 42(6): 961–969.

[14] TIAN Wei, PEI Zhi-ru, HAN Nü. A preliminary research on three-dimensional reconstruction and mechanical characteristics of rock mass based on CT scanning and 3D printing technology[J]. Rock and Soil Mechanics, 2017, 38(8): 2297–2305.

[15] GELL E M, WALLEY S M, BRAITHWAITE C H. Review of the validity of the use of artificial specimens for characterizing the mechanical properties of rocks[J]. Rock Mechanics and Rock Engineering, 2019, 52(9): 2949–2961.

[16] YANG Yong-ming, JU Yang, WANG Hui-jie. Physical model and failure analysis of porous rock[J]. Chinese Journal of Geotechnical Engineering, 2010, 32(5): 736–744.

[17] LI Jing, KONG Xiang-chao, SONG Ming-shui, et al. Study on the influence of reservoir rock micro-pore structure on rock mechanical properties and crack propagation[J]. Rock and Soil Mechanics, 2019, 40(11): 4149–4156.

[18] CHENG Zhi-lin, SUI Wei-bo, NING Zheng-fu, et al. Microstructure characteristics and its effects on mechanical properties of digital core[J]. Chinese Journal of Rock Mechanics and Engineering, 2018, 37(2): 449–460.

[19] JIANG Ming-jing, ZHANG Ning, CHEN He. Discrete element simulation of aging effect of chemical weathering on rock[J]. Rock and Soil Mechanics, 2014, 35(12): 3577–3584.

[20] WU Z J, ZHANG B, WENG L, et al. A new way to replicate the highly stressed soft rock: 3D printing exploration[J]. Rock Mechanics and Rock Engineering, 2020, 53(1): 467–476.

[21] MOSTAFAEI A, ELLIOTT A M, BARNES J E, et al. Binder jet 3D printing—process parameters, materials, properties, modeling, and challenges[J]. Progress in Materials Science, 2021, 119: 100707.

[22] WU Y, MCGARRY F J, ZHU B, et al. Temperature effect on mechanical properties of toughened silicone resins[J]. Polymer Engineering & Science, 2005, 45(11): 1522–1531.

[23] ZHOU T, ZHU J B. Identification of a suitable 3D printing material for mimicking brittle and hard rocks and its brittleness enhancements[J]. Rock Mechanics and Rock Engineering, 2018, 51(3): 765–777.

[24] SONG Zhao-yang, JI Hong-guang, ZENG Peng, et al. Phase-like transition characteristics of uniaxial compression failure of weakly cemented coarse-grained sandstone in western china[J]. Journal of Mining and Safety Engineering, 2020, 37(5): 1027–1036.

[25] SONG Zhao-yang, JI Hong-guang, ZHANG Yue-zheng, et al. Acoustic emission signal sources and critical failure precursors of weakly consolidated sandstone with different grain sizes[J]. Journal of China Coal Society, 2020, 45(12): 4028–4036.

[26] JIA Peng, YANG Qi-yao, LIU Dong-qiao, et al. Physical and mechanical properties and related microscopic characteristics of high-temperature granite after water-cooling[J]. Rock and Soil Mechanics, 2021, 42(6): 1568–1578.

[27] WU Yang-chun, XI Bao-ping, WANG Lei, et al. Experimental study on physico-mechanical properties of granite after high temperature[J]. Journal of Central South University (Science and Technology), 2020, 51(1): 193–203.

[28] MENG Ling-chao, XU Rong-chao, WANG An-ming, et al. Characteristics of strength and acoustic emission of granite and marble under uniaxial compression[J]. Journal of Engineering Geology, 2020, 28(6): 1178–1185.

[29] FERESHTENEJAD S, SONG J J. Fundamental study on applicability of powder-based 3D printer for physical modeling in rock mechanics[J]. Rock Mechanics and Rock Engineering, 2016, 49(6): 2065–2074.